nature communications

Article

https://doi.org/10.1038/s41467-024-47973-3

Coherent electric field control of orbital state of a neutral nitrogen-vacancy center

Received: 18 August 2023

Accepted: 17 April 2024

Published online: 13 May 2024

Check for updates

Hodaka Kurokawa[1] ✉, Keidai Wakamatsu[2], Shintaro Nakazato[2], Toshiharu Makino[1,3], Hiromitsu Kato[1,3], Yuhei Sekiguchi[1] & Hideo Kosaka[1,3] ✉

The coherent control of the orbital state is crucial for realizing the extremely-low power manipulation of the color centers in diamonds. Herein, a neutrally-charged nitrogen-vacancy center, NV^0, is proposed as an ideal system for orbital control using electric fields. The electric susceptibility in the ground state of NV^0 is estimated, and found to be comparable to that in the excited state of NV^-. Also, the coherent control of the orbital states of NV^0 is demonstrated. The required power for orbital control is three orders of magnitude smaller than that for spin control, highlighting the potential for interfacing a superconducting qubit operated in a dilution refrigerator.

Diamond color centers are attracting increased attention because of their potential applications in quantum communication[1–3], quantum computation[4,5], and quantum sensing[6,7]. The spin degree of freedom is primarily utilized as a quantum bit owing to its long coherence time of over 1 s[8–10], and excellent controllability[11,12]. However, the control of the orbital degree of freedom is also crucial for various applications such as the frequency tuning of the zero-phonon line photons and extremely low-power control of the electron states. The ability to tune the zero-phonon line frequency through electric fields or strain is essential for generating entanglement between remote color centers[1,13,14]. Moreover, the coupling of electric fields or strain with the orbital degree of freedom is stronger compared to the magnetic field's coupling with the spin[15–17], allowing the highly efficient control of the electron state. Owing to the strong spin-orbit coupling, efficient spin-state control using the strain has been achieved in color centers[18], which is particularly advantageous for operations in a dilution refrigerator. Nevertheless, directly achieving coherent control over the orbital state remains challenging for representative color centers owing to the short lifetime of the optically excited state of NV^- (~10 ns)[19] and large ground-state splitting of group-IV color centers[20].

Therefore, a neutrally charged nitrogen-vacancy center, NV^0 [21–31], is proposed herein as an ideal system for orbital state control using electric fields. The ground-state spin-orbit splitting of NV^0 is ~10 GHz[27,28], allowing direct microwave access. Additionally, the ground state of NV^0 exhibits an orbital relaxation time of several hundreds of nanoseconds[28], which is more than one order of magnitude longer than that of the excited state of NV^-. The energy level structure of the ground state in NV^0 is also similar to that of group-IV color centers. Therefore, NV^0 can serve as an ideal system for understanding the properties of the orbital state and conducting proof-of-principle experiments relevant to group-IV color centers. In this study, the electric susceptibility of NV^0 is investigated, and the coherent control of its orbital state is demonstrated. The highly-efficient control of the electron state creates possibilities for future applications, such as in a quantum interface communicating with a superconducting quantum bit in a dilution refrigerator[32,33].

Results

Characterization of NV^0

Under a zero magnetic field, the ground-state Hamiltonian, H, of NV^0 in the $|\pm\rangle_o$ basis can be modeled as[27,28]:

$$H^{(\pm)}/h = 2\lambda \hat{L}_z \hat{S}_z + \epsilon_\perp (\hat{L}_+ + \hat{L}_-), \quad (1)$$

where h is the Plank's constant, λ is the spin-orbit interaction parameter, $\hat{L}_z = \hat{\sigma}_z$, and $\hat{L}_\pm = |\pm\rangle_o\langle\mp|_o$ are the orbital operators in the $|\pm\rangle_o = \mp 1/\sqrt{2}(|e_x\rangle_o \pm i|e_y\rangle_o)$ basis, $|e_x\rangle_o$ and $|e_y\rangle_o$ are the strain eigenstates, $\hat{S}_z = (1/2)\hat{\sigma}_z$ is the spin operator for 1/2 spin, and $\epsilon_\perp$ is

[1]Quantum Information Research Center, Institute of Advanced Sciences, Yokohama National University, 79-5 Tokiwadai, Hodogaya, Yokohama 240-8501, Japan. [2]Department of Physics, Graduate School of Engineering Science, Yokohama National University, 79-5 Tokiwadai, Hodogaya, Yokohama 240-8501, Japan. [3]Advanced Power Electronics Research Center, National Institute of Advanced Industrial Science and Technology, 1-1-1 Umezono, Tsukuba, Ibaraki 305-8568, Japan. ✉e-mail: kurokawa-hodaka-hm@ynu.ac.jp; kosaka-hideo-yp@ynu.ac.jp

the perpendicular strain parameter. Moreover, the subscript, o, denotes the orbital degree of freedom. Figure 1a shows the energy level of NV^0. The ground-state splitting originates from the spin-orbit coupling, λ, and the strain, $\epsilon_\perp$, as $2\sqrt{\lambda^2+\epsilon_\perp^2}$. Under strain, the eigenstates change from $|\pm\rangle_o$ to $|+'\rangle_o = \alpha|+\rangle_o + \beta|-\rangle_o$ and $|-'\rangle_o = -\beta|+\rangle_o + \alpha|-\rangle_o$ with $\alpha^2+\beta^2=1$ (See Supplementary Eqs. (9)(10)). Figure 1b shows the electrical circuit directly formed on a diamond. Low- (<1 MHz) and high-frequency (~10 GHz) electric fields are applied to the nitrogen vacancies using the upper electrodes. The color map of the photoluminescence (PL) counts around the center of the circuit is also shown. Figure 1c shows the photoluminescence excitation (PLE) spectrum with the experimental sequence. A 637 nm red laser resonant to the zero-phonon line (ZPL) of NV^- is used to convert NV^- to NV^0. The frequencies of a 575 nm yellow laser are then swept to search for the ZPL of NV^0. Consequently, two transition lines are observed, which indicates that the ground-state splitting is 12.85 GHz.

Since all experiments are performed under an ambient magnetic field, the transitions from $|+'\rangle_o|\uparrow\rangle_s$ and $|-'\rangle_o|\downarrow\rangle_s$ are indistinguishable, where the subscript, s, denotes the spin degree of freedom. Additionally, $|-'\rangle_o|\uparrow\rangle_s$ and $|+'\rangle_o|\downarrow\rangle_s$ are indistinguishable. These states can be rewritten as $|-'\rangle_o|\uparrow\rangle_s = |+'\rangle_o|\downarrow\rangle_s \equiv |0\rangle$, $|+'\rangle_o|\uparrow\rangle_s = |-'\rangle_o|\downarrow\rangle_s \equiv |1\rangle$, and $|0\rangle_o|\uparrow\rangle_s = |0\rangle_o|\downarrow\rangle_s \equiv |2\rangle$ by ignoring the spin degree of freedom. In other words, the four-level system in the ground state is treated as effective two-level systems with different spin states. This assumption holds for spin-independent experiments or experiments with time scales shorter than spin relaxation time. Basically, our experiments are assumed to be spin-independent because we can drive and readout both spin states optically and electrically. Furthermore, although reported spin relaxation times range from 570 μs to 1.5 s depending on situations[28,34], they are still longer than the timescale of our experiments (~a few μs).

Subsequently, DC electric fields are applied to estimate the parameters in Equation (1) and the electric susceptibility. The effects of both the strain and DC electric fields in the $|\pm\rangle_o|\uparrow\rangle_s$ basis can be expressed as:

$$H^{(\pm)}/h = \lambda\hat{L}_z + d_\parallel E_z\hat{I} + (\epsilon_\perp + d_\perp E_\perp)(\hat{L}_+ + \hat{L}_-) + d_\perp E'(-i\hat{L}_+ + i\hat{L}_-), \quad (2)$$

where $d_\parallel (d_\perp)$ is the electric susceptibility parallel (perpendicular) to the NV axis, E_z is the electric fields parallel to the NV axis, $E_\perp$ is the electric fields whose axis is parallel to the direction of $\epsilon_\perp$, and $E'_\perp$ is the electric fields perpendicular to $E_\perp$ and E_z. Here, the strain term which only contributes to the global shift of the energy is ignored (See Supplementary Notes). The energy eigenvalues are $d_\parallel E_z \pm \sqrt{\lambda^2 + (\epsilon_\perp + E_\perp)^2 + (d_\perp E'_\perp)^2}$. Figure 1d shows the PLE frequency shifts at both the upper ($|1\rangle$) and lower ($|0\rangle$) branches as a function of the DC electric fields. With increasing DC electric fields, the PLE frequencies of the two branches decrease almost linearly. Additionally, with the application of ± 50 V, the PLE frequencies can be shifted up to ~30 GHz. The linear frequency shifts in both branches are caused by E_z. Using the electric field distribution obtained from the finite element simulation, $d_\parallel$ is estimated to be 1.08 MHz/(V cm^{-1}) (See Supplementary Methods), which is similar to the reported value in the excited state of NV^- of 0.7 MHz/(V cm^{-1})[17]. The frequency shifts owing to $E_\perp$ and $E'_\perp$ can be clearly seen by subtracting the upper PLE frequencies from the lower PLE frequencies (Inset of Fig. 1d). The frequency differences are then fitted using the equation $2\sqrt{\lambda^2 + (\epsilon_\perp + d_\perp E_\perp)^2 + (d_\perp E'_\perp)^2}$ and a fixed $\lambda = 4.90$ GHz based on the value in ref. 28. Consequently, the estimated parameters are $\epsilon_\perp = 3.92$ GHz and $d_\perp = 358\ (14)$ kHz/(V cm^{-1}). It should be noted that $d_\perp$ is several times smaller than the value reported in ref. 17 for the excited state of NV^-, 1.4 MHz/(V cm^{-1}).

Orbital relaxation of NV^0

The orbital relaxation time, T_1, is important because it determines the limit of the operation time. Figure 2a shows the experimental sequence

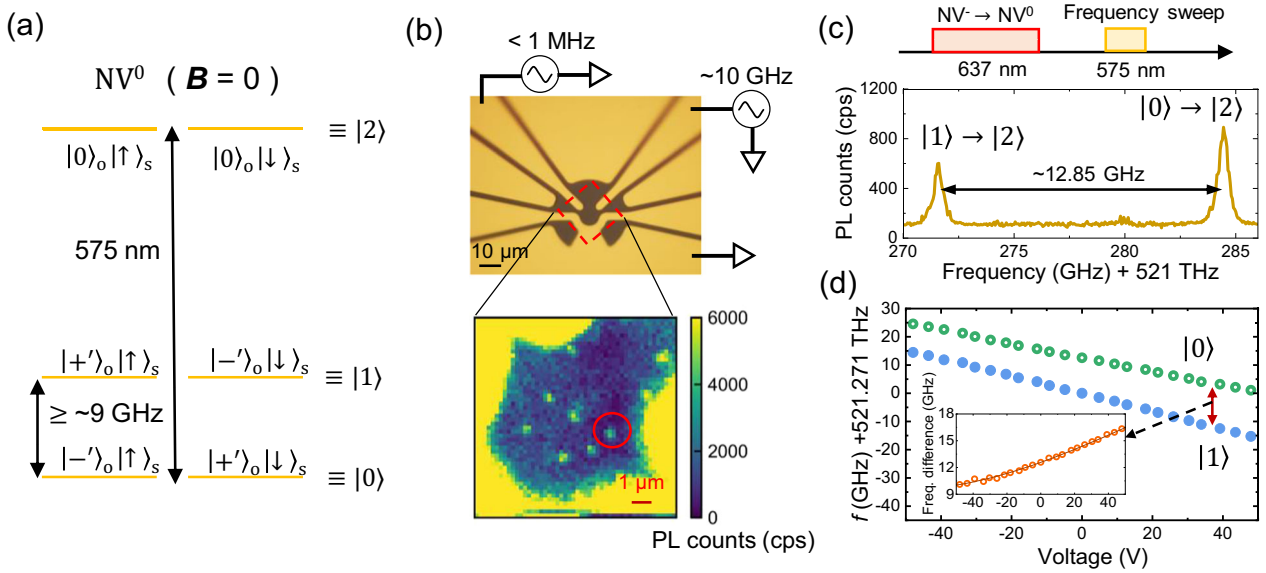

Fig. 1 | Energy level structure of NV^0, device image, photoluminescence excitation (PLE) spectrum, and DC voltage dependence of the PLE spectrum. **a** Schematic of the energy level of NV^0 with some static strain under a zero magnetic field. The ground state exhibits energy splitting in the order of 10 GHz owing to the combined effects of spin-orbit interaction and strain. Moreover, the optical transition occurs at 575 nm. **b** Optical microscope image of the electrical circuit on the diamond used in the experiments. The upper electrodes are used to apply low (<1 MHz) or high (~10 GHz) electric fields. Moreover, the color map shows the photoluminescence (PL) counts around the center of the circuit. The red-circled NV center is used for experiments. **c** PLE spectrum of NV^0 and its measurement sequence. The 637 nm laser resonant at the zero-phonon line of NV^- is used to initialize the charge state to NV^0, and the 575 nm laser is used to observe the transition. **d** PLE spectrum shifts as a function of the DC voltage. The green and blue circles correspond to the lower ($|0\rangle$) and upper ($|1\rangle$) branches, respectively, and the inset shows the difference in the PLE frequencies of the upper ($|0\rangle$) and lower ($|1\rangle$) branches. Additionally, the horizontal axis is the same as that of the main graph.

https://doi.org/10.1038/s41467-024-47973-3

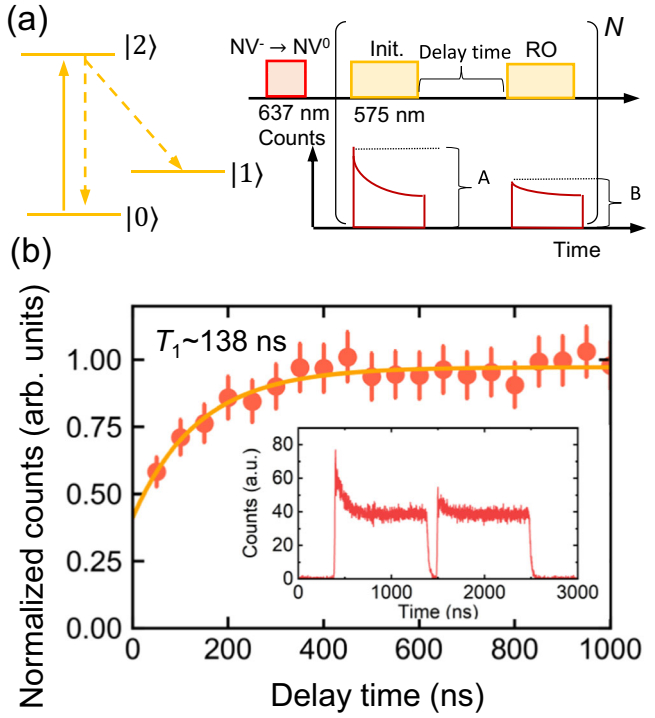

Fig. 2 | Measurement of the orbital relaxation time of NV⁰. a Schematic of the experimental sequence for measuring the orbital relaxation time of NV⁰. After charge initialization (Init.) using the 637 nm laser, the first 575 nm laser pulse initializes $|0\rangle$ to $|1\rangle$, and the population in $|0\rangle$ is read out (RO) by the second 575 nm pulse after some delay time. The peak counts, *A* and *B*, at each pulse are used to estimate the population in $|0\rangle$. The repetition time for each measurement, *N*, is 150, and is determined by measuring the decay of the PL counts as a function of the duration of the 575 nm laser irradiation. **b** Normalized counts, *B*/*A*, as a function of the delay time. The red dots are the experimental data and the orange curve is the results of curve fitting using the exponential function. The inset shows the time-resolved PL counts of two pulses with a 100 ns gap in between. Additionally, the PL counts are smoothed using the Savitzky-Golay filter with 17 points before the calculation of the peak height, and the background is subtracted using the data when the laser is absent. Error bars correspond to standard deviation error after the smoothing.

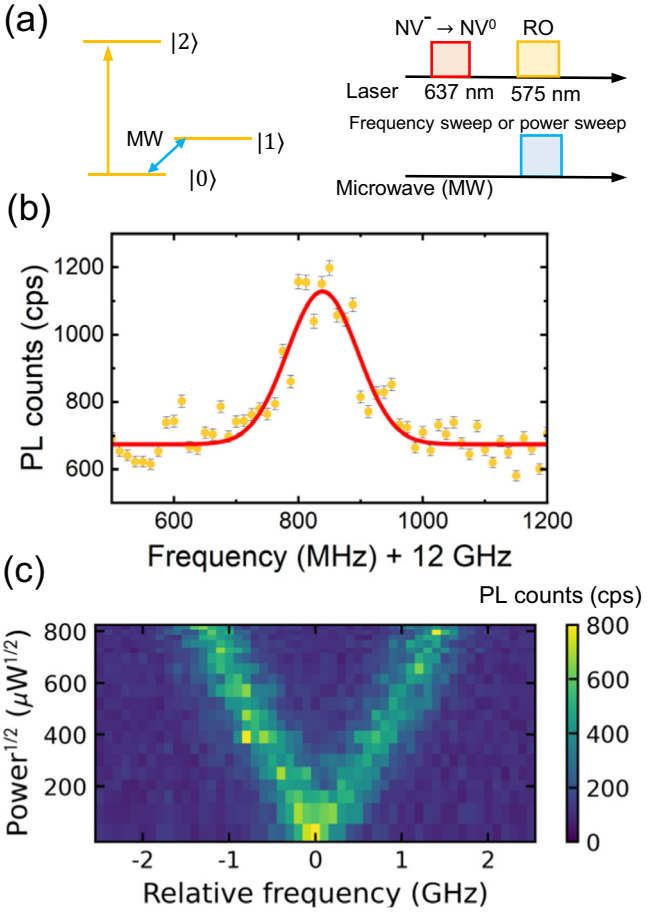

Fig. 3 | Optically detected electrical resonance (ODER) and the Autler-Townes splitting measurements. a Schematic of the experimental sequence used in measuring the ODER and the Autler-Townes splitting. After charge conversion using the 637 nm laser, the 575 nm laser is simultaneously applied with microwave application at the transition between $|0\rangle$ and $|2\rangle$. The microwave frequencies are then swept for ODER measurement, and the power of the microwave is swept for the measurement of the Autler-Townes splitting. **b** ODER spectrum of NV⁰. The orange dots represent the data and the red curve is the Gaussian fit. Error bars correspond to standard deviation error. **c** The Autler-Townes splitting as a function of the square root of the power of the applied microwave electric fields.

for the measurement of T_1. A 1 μs long optical pulse resonant is applied to the transition between $|0\rangle$ and $|2\rangle$ to initialize NV⁰ into $|1\rangle$ from the thermal mixture of $|0\rangle$ and $|1\rangle$ (Inset of Fig. 2b). The first peak height is proportional to the initial population in $|0\rangle$, and the peak height in the second pulse is proportional to the population in $|0\rangle$ relaxed from $|1\rangle$. The ratio of the pulse heights in the first and second pulses is a measure of the decay from $|1\rangle$, and was used to calculate T_1. Figure 2b shows the normalized pulse height as a function of the delay of the second pulse. T_1 is estimated to be ~138 (19) ns at 5.5 K based on the curve fit with $1 - a\exp(-t/T_1) + b$, where a and b are constants. In ref. 28, T_1 is a few times larger than ours. Since T_1 is limited by thermal phonons at 5.5 K, a further increase in T_1 is expected by lowering the temperature to several tens of millikelvin.

Optically detected electrical resonance and the Autler-Townes splitting

To investigate the electrical resonance frequency in the ground state of NV⁰, the optically detected electrical resonance (ODER) is employed. Since the driving electric field is resonant to the eigenfrequency determined by λ and $\epsilon_\perp$, the AC driving electric fields is treated as a perturbation to $|\pm'\rangle_o$ which is the eigenstates of Equation (1). In the rotating frame of the driving AC electric fields, $H_d/h = f_d\hat{L}_z/2$, under the rotating wave approximation, the Hamiltonian of NV⁰ in the $|\pm'\rangle_o$ basis can be written as:

$$H^{(\pm')}/h = \frac{\Delta}{2}\hat{L}_z + \frac{d_\perp E''_\perp}{2}(\hat{L}_+ + \hat{L}_-), \quad (3)$$

where f_d is the frequency of the driving electric fields, $\Delta = 2\sqrt{\lambda^2 + \epsilon_\perp^2} - f_d$ is the detuning, $E''_\perp = \sqrt{(\alpha^2 - \beta^2)E_x^2 + E_y^2}$ represents the electric fields perpendicular to the NV axis, and E_x and E_y are the in-plane electric fields (See Supplementary Notes). Here, $\hat{L}_\pm$ are the rising (lowering) operators in the $|\pm'\rangle_o$ basis. When $\Delta \sim 0$, the second term that remains in Equation (3) contributes to the Autler-Townes splitting and Rabi oscillation, which will be discussed in below.

Figure 3a shows the experimental sequence. The microwave frequencies are swept around the frequency resonant to the transition between $|0\rangle$ and $|1\rangle$, which is roughly estimated from the PLE measurement. Simultaneously, the readout laser is applied to measure the population in $|0\rangle$. A sufficiently long readout pulse increases the population in $|1\rangle$ through optical pumping, as shown in the inset of Fig. 2b. When the microwave frequency and ground-state splitting are in resonance, the population in $|1\rangle$ is transferred to $|0\rangle$, resulting in an

https://doi.org/10.1038/s41467-024-47973-3

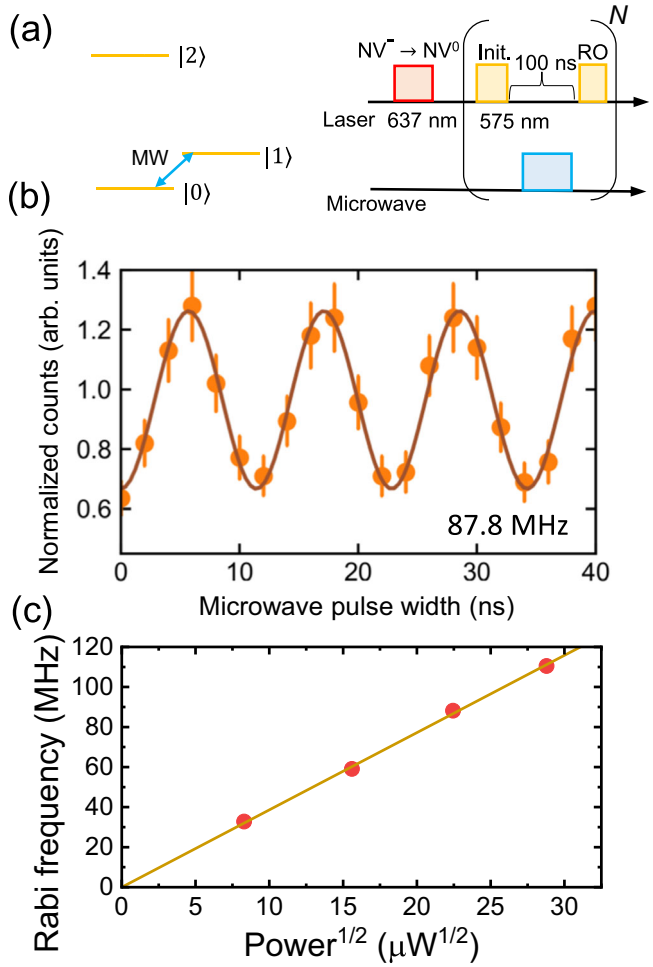

Fig. 4 | Rabi oscillation and microwave power dependence of the Rabi frequency. a Schematic of the experimental sequence for Rabi oscillation. The microwave pulse is applied between the first (initialization) and second (readout) laser pulses, and the microwave frequency is set to the resonance frequency obtained from ODER measurement. The repetition times, *N*, are 100. **b** Normalized counts as a function of the microwave pulse width. The orange dots represent the data and the brown curve is the cosinusoidal fit. Error bars correspond to standard deviation error. The Rabi frequency is 87.8 MHz. **c** Rabi frequency as a function of the square root of the input power. The slope is 3.86 MHz/μW$^{1/2}$.

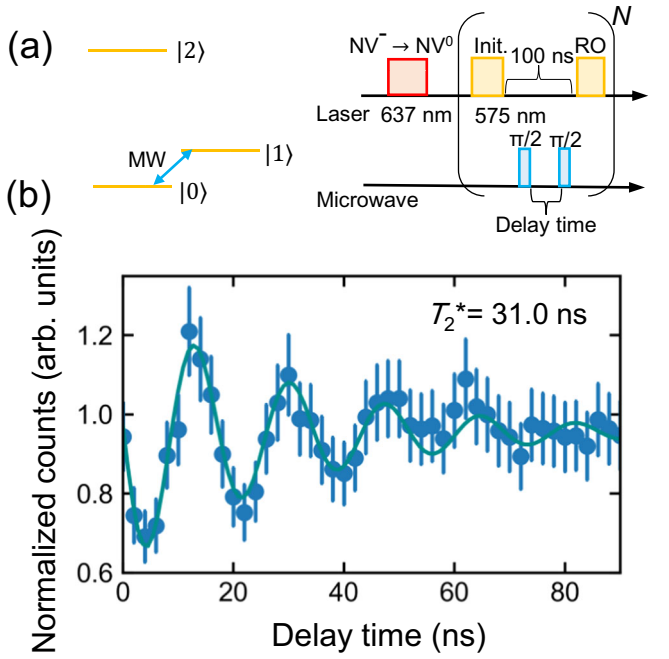

Fig. 5 | Ramsey interference. a Schematic of the experimental sequence for Ramsey interference, where the two microwave pulses are applied between the first (initialization) and second (readout) laser pulses. The microwave width for the $\pi/2$ pulse is determined to be 4.6 ns based on the Rabi oscillation measurement. The repetition times, *N*, are 100. **b** Normalized counts as a function of the delay time of the microwave pulse (free precession time). The blue dots represent the data and the blue curve represents the fitting using the function, $A\sin(\Delta t+\phi)\exp(-t/T_2^*)+B$, where A, B, and ϕ are constants, Δ is the detuning from the transition between $|0\rangle$ and $|1\rangle$, and T_2^* is the orbital coherence time. Error bars correspond to standard deviation error. T_2^* is 31.0 ns.

increase in the PL counts. Figure 3b shows the results of the ODER measurement. The maximum of the spectrum is 12.84 GHz, which is in good agreement with the ground-state splitting obtained from the PLE measurement. Additionally, the full width at half maximum (FWHM) is 133 (10) MHz due to the spectral diffusion in the ground and optically excited states.

Using the resonance frequency (12.84 GHz) obtained from the ODER measurement, the microwave power dependence of the Autler-Townes splitting is investigated by increasing the microwave power. The Autler-Townes splitting originates from the formation of the color center-field dressed states because of the strong driving field (See Supplementary Notes). The splitting between the two peaks corresponds to $d_\perp E''_\perp$, the Rabi frequency. Figure 3c shows the color map of the PL counts as functions of the relative frequency and square root of the microwave power. The maximum Autler-Townes splitting is 2.6 GHz at 824 μW$^{1/2}$. The power dependence of Autler-Townes splitting directly corresponds to the power dependence of the Rabi frequency, which is estimated to be 3.37 MHz/μW$^{1/2}$ via fitting. Additionally, the electric susceptibility is estimated to be $d_\perp^{AC}$ = 1.0 MHz/(V cm^{-1}) (See Supplementary Methods). Here, $d_\perp^{AC}$ is larger than that obtained from the measurement using DC electric fields (358 kHz/(V cm^{-1})). The difference can be attributed to electric field screening during DC measurement, which decreases the effective electric fields at the NV center[17]. The value of $d_\perp^{AC}$ is in relatively good agreement with that of the optically excited state of NV$^-$, which is 1.4 MHz/(V cm^{-1})[17].

Rabi oscillation and Ramsey interference

Using the resonance frequency obtained from ODER measurement, the Rabi oscillations between $|0\rangle$ and $|1\rangle$ are observed. Figure 4a shows the experimental sequence for measurement, where the microwave pulse is applied between the two laser pulses. Figure 4b shows the Rabi oscillation at an input microwave power of 504 μW, where the Rabi frequency is 87.8 MHz. Compared to the power required to drive a spin of NV$^-$ at a similar distance from the electrode (several μm), the required power is three orders of magnitude smaller. Figure 4c shows the Rabi frequency as a function of the square root of the microwave power. Here, the Rabi frequency linearly increases with the square root of the microwave power, and the slope is 3.86 (3) MHz/μW$^{1/2}$, which is in good agreement with the value obtained from the Autler-Townes splitting measurement of 3.37 MHz/μW$^{1/2}$.

The coherence time, T_2^*, of the orbital state is also investigated using the Ramsey interference. Figure 5a shows the experimental sequence. The two microwave $\pi/2$ pulses are applied between the initializing and readout laser pulses. Figure 5b shows the Ramsey interference with some detuning as a function of the free precession time. Based on curve fitting, the detuning is 58 MHz and T_2^* is 31.0 (3.6) ns. The origins of the decoherence are attributed spectral diffusion[35] in the ground state and thermal phonons that are resonant with the orbital transition proposed for SiV[36]. The value of T_2^* is similar

to the spin coherence time of SiV at ~5 K (30–50 ns)[18,37,38]. Thus, a further increase in T_2^* is expected by decreasing the temperature and the application of the dynamical decoupling as SiV.

Discussion

The electric susceptibility of NV^0 has been measured in the ground state, and found to be comparable to that in the excited state of NV^-. Additionally, the coherent control of the orbital state of NV^0 has been achieved using electric fields. The required power for Rabi oscillation is hundreds of microwatts, which is three orders of magnitude smaller than that required for spin control using magnetic fields (See Supplementary Discussion).

The highly efficient control of the orbital state is particularly advantageous for the operations in a dilution refrigerator, opening up the possibility for interfacing a superconducting qubit and a color center via electric fields. If a high impedance superconducting microwave resonator with a zero-point voltage fluctuation of tens of microvolts[39,40] is integrated, the single-photon coupling is expected to be tens of kilohertz, allowing further low-power microwave control using several hundred microwave photons. If we can further increase the coupling to ~1 MHz by bringing the electrode and the color center closer together, we can reach the strong coupling regime of the color center and the microwave resonator, where we can observe single-photon interaction.

Also, we should compare the electric field control of the orbital state with another driving scheme, mechanical driving[18]. The electric field driving requires less complex devices and offers wide frequency range while typical mechanical oscillators employed in experiments are mechanical resonators with narrow frequency range around resonant frequency[16,18]. However, though device fabrication processes and frequency tuning result in some more complexity in experiments, controlling the orbital state using phonons is still promising. Since the mode volume of the phononic resonator can be designed to be several orders of magnitude smaller than that of typical microwave resonators[32,41], the single-phonon coupling can exceed 1 MHz without the use of extremely close proximity electrodes as mentioned above, allowing to reach the strong coupling regime with maintaining both microwave and optical access.

In addition, a comparison with group IV color centers needs to be discussed. Although the ground state can be modeled with the same Hamiltonian for NV^0 and group IV color centers, considering the spin-orbit coupling, the spin (orbital) Zeeman effect, the strain, and the Jahn-Teller effect which is indistinguishable from strain, the coefficients in each term are different. The largest difference in parameters would be the spin-orbit coupling, which ranges from ~5 GHz in NV^0 to ~400 GHz (corresponding to the splitting of ~800 GHz) in PbV. The ratio of spin-orbit coupling to strain determines the degree of hybridization of the ground state wavefunction, which is essential for magnetic field control of the ground state spin. For NV^0 with 5 GHz spin-orbit coupling, several GHz to tens of GHz of strain parameters are sufficient to fully tune its wavefunction from the spin-orbit coupling dominant regime to the strain dominant regime. In contrast, tens to hundreds of GHz of strain are required to fully control the wavefunction of group IV color centers. Furthermore, we can control the Hamiltonian of NV^0 using DC electric fields, effectively suppressing or enhancing the effect of static strain. Thus, NV^0 can be a good platform to study the effect of strain on the Hamiltonian in a wide parameter range with relatively small strain parameters and DC electric fields. It should be noted that the excited state Hamiltonian of NV^0 and group IV color centers are different. While NV^0 has two optically excited states with two spin degrees of freedom and one orbital degree of freedom, group IV color centers have optically excited states with two spin degrees of freedom and two orbital degrees of freedom. This difference may affect the readout scheme when considering the single-photon readout demonstrated in ref. 12.

Although the measured T_1 is 138 ns at 5.5 K, it is expected to extend to microseconds in the dilution refrigerator environment due to a decrease in the thermal phonons. If it reaches several microseconds, it can be used as an interface between the superconducting quantum bit[33], which is proposed for the silicon-vacancy center[32]. Despite of the several challenges posed by spectral diffusion, the integration of the microwave resonator, and operations in the dilution refrigerator, this study demonstrates a promising path for hybrid quantum systems.

Methods

Sample fabrication

[100]-cut electronic-grade single-crystal diamond samples are synthesized via chemical vapor deposition (CVD) (element six). Before the fabrication of the electrode, the diamond substrate is kept in a mixture of H_2SO_4 and HNO_3 at 200°C for 60 min to remove any surface contamination and terminate the surface with oxygen. Subsequently, Au (500 nm)/Ti (10 nm) electrodes are formed on the substrate through photolithography processes.

Low-temperature confocal microscopy

All experiments are performed in a closed-cycle optical cryostat (Cryostation s50, Montana Instruments) at 5.5 K under an ambient magnetic field. A copper sample holder is mounted on the XYZ piezoelectric nanopositioners (ANP x 101 × 2, ANPz101) using a thermal link, and the diamond sample is fixed onto a homemade printed circuit board (PCB) using aluminum tapes. Additionally, the electrodes on the diamond are connected to the PCB using gold wire bonds, and the PCB is attached to the sample holder using screws.

Optical excitation and collection are then performed using a home-built confocal microscope. An objective lens (LMPLFLN100X, Olympus), whose numerical aperture is 0.8, is scanned over the sample using a XYZ piezoelectric nanopositioner (P-517.3CD, Physik Instrumente).

A 515 nm green laser (Cobolt, Hubner Photonics) is used for off-resonant excitation to search for the nitrogen-vacancy centers, and a 575 nm yellow laser (DL-SHG pro, Toptica Photonics) is used to resonantly excite NV^0 for initialization and readout. Typically, a 1-μs pulse is used and the power is 1 μW. A 637 nm red laser (DL pro, Toptica Photonics) is also used to resonantly excite NV^- to convert it from the negatively charged state to the neutrally charged state. The pulse width for charge initialization is 100 μs and the power is 200 μW. The charge initialization fidelity is estimated to be >97.0% from the residual fluorescence after the irradiation of long charge initialization pulse. Each laser is directed along the main optical path using dichroic mirrors (FF552-Di02-25 × 36: 515 nm, FF605-Di02-25 × 36: 575 nm, FF649-Di01-25 × 36: 637 nm, Semrock) after being purified through bandpass filters (FF02-520/28-25: 515 nm, FF03-575/25-25: 575 nm, FF01-637/7-25: 637 nm, Semrock).

The power of the 515 nm laser is controlled by setting the internal output power, and those of the 575 nm and 637 nm lasers are controlled using variable fiber-optic attenuators (V450PA: 575 nm, V600PA: 637 nm, Thorlabs). Additionally, the pulse duration of the 515 nm laser is directly set based on the signal sent from a field programmable gate array (FPGA). The pulse durations of the 575 nm and 637 nm laser are gated using acousto-optic modulators (SFO4903-S-M200 0.4C2C-3-F2P-01: 575 nm, SFO3916-S-M200-0.4C2E-3-F2P-02: 637 nm, Gooch and Housego) controlled by the FPGA (PXIe-7820R, National Instruments).

The phonon sideband of NV^0 and NV^- is collected and measured using a single-photon counter (SPCM-AQRH-14-FC, Excelitas). For the time-resolved photoluminescence measurements, the signal from the single-photon counter is sent to a time-resolved single-photon counter (Picoharp300, PicoQuant) and the time-bin is set to be 512 ps.

DC and AC electronics for measurements

The DC voltages are generated using an arbitrary waveform generator (M3202A, Keysight), and the voltages are amplified using amplifiers (EVAL-ADHV4702-1CPZ, Analog Devices). The microwave voltages of up to 16 GHz (>25 GHz for a single channel) are generated using another arbitrary waveform generator (M8195A, Keysight), and the microwave voltages are amplified using an amplifier (ZVE-3W-183+, Mini Circuits). Additionally, the microwave power at the sample is estimated using a network analyzer (P9373A, Keysight). The loss inside the cryostat is estimated from the reflection coefficient, S_{11}, inside the cryostat. Assuming equal energy loss on the way to the sample and back, half of S_{11} corresponds to the loss between the input port and sample.

Data availability

All data generated in this study are presented in the main text and the supplementary information. The source data generated in this study have been deposited in Figshare under accession code: https://doi.org/10.6084/m9.figshare.25017170[42].

References

1. Bernien, H. et al. Heralded entanglement between solid-state qubits separated by three metres. *Nature* **497**, 86–90 (2013).
2. Pompili, M. et al. Realization of a multinode quantum network of remote solid-state qubits. *Science* **372**, 259–264 (2021).
3. Bhaskar, M. K. et al. Experimental demonstration of memory-enhanced quantum communication. *Nature* **580**, 60–64 (2020).
4. Nemoto, K. et al. Photonic architecture for scalable quantum information processing in diamond. *Phys. Rev. X* **4**, 031022 (2014).
5. Abobeih, M. H. et al. Atomic-scale imaging of a 27-nuclear-spin cluster using a quantum sensor. *Nature* **576**, 411–415 (2019).
6. Dolde, F. et al. Electric-field sensing using single diamond spins. *Nat. Phys.* **7**, 459–463 (2011).
7. Degen, C. L., Reinhard, F. & Cappellaro, P. Quantum sensing. *Rev. Mod. Phys.* **89**, 035002 (2017).
8. Balasubramanian, G. et al. Ultralong spin coherence time in isotopically engineered diamond. *Nat. Mater.* **8**, 383–387 (2009).
9. Bar-Gill, N., Pham, L. M., Jarmola, A., Budker, D. & Walsworth, R. L. Solid-state electronic spin coherence time approaching one second. *Nat. Commun.* **4**, 1743 (2013).
10. Abobeih, M. H. et al. One-second coherence for a single electron spin coupled to a multi-qubit nuclear-spin environment. *Nat. Commun.* **9**, 2552 (2018).
11. Abobeih, M. H. et al. Fault-tolerant operation of a logical qubit in a diamond quantum processor. *Nature* **606**, 884–889 (2022).
12. Nguyen, C. T. et al. Quantum network nodes based on diamond qubits with an efficient nanophotonic interface. *Phys. Rev. Lett.* **123**, 183602 (2019).
13. Tamarat, P. et al. Spin-flip and spin-conserving optical transitions of the nitrogen-vacancy centre in diamond. *N. J. Phys.* **10**, 045004 (2008).
14. Maze, J. R. et al. Properties of nitrogen-vacancy centers in diamond: the group theoretic approach. *N. J. Phys.* **13**, 025025 (2011).
15. Meesala, S. et al. Strain engineering of the silicon-vacancy center in diamond. *Phys. Rev. B* **97**, 205444 (2018).
16. Chen, H. Y., MacQuarrie, E. R. & Fuchs, G. D. Orbital state manipulation of a diamond nitrogen-vacancy center using a mechanical resonator. *Phys. Rev. Lett.* **120**, 167401 (2018).
17. Block, M. et al. Optically enhanced electric field sensing using nitrogen-vacancy ensembles. *Phys. Rev. Appl.* **16**, 024024 (2021).
18. Maity, S. et al. Coherent acoustic control of a single silicon vacancy spin in diamond. *Nat. Commun.* **11**, 193 (2020).
19. Batalov, A. et al. Temporal coherence of photons emitted by single nitrogen-vacancy defect centers in diamond using optical rabi-oscillations. *Phys. Rev. Lett.* **100**, 077401 (2008).
20. Wolfowicz, G. et al. Qubit guidelines for solid-state spin defects. *Nat. Rev. Mater.* **6**, 906–925 (2020).
21. Manson, N. B. & Harrison, J. P. Photo-ionization of the nitrogen-vacancy center in diamond. *Diam. Relat. Mater.* **14**, 1705–1710 (2005).
22. Gali, A. Theory of the neutral nitrogen-vacancy center in diamond and its application to the realization of a qubit. *Phys. Rev. B* **79**, 235210 (2009).
23. Hauf, M. V. et al. Chemical control of the charge state of nitrogen-vacancy centers in diamond. *Phys. Rev. B* **83**, 081304 (2011).
24. Grotz, B. et al. Charge state manipulation of qubits in diamond. *Nat. Commun.* **3**, 729 (2012).
25. Siyushev, P. et al. Optically controlled switching of the charge state of a single nitrogen-vacancy center in diamond at cryogenic temperatures. *Phys. Rev. Lett.* **110**, 167402 (2013).
26. Doi, Y. et al. Deterministic electrical charge-state initialization of single nitrogen-vacancy center in diamond. *Phys. Rev. X* **4**, 011057 (2014).
27. Barson, M. S., Krausz, E., Manson, N. B. & Doherty, M. W. The fine structure of the neutral nitrogen-vacancy center in diamond. *Nanophotonics* **8**, 1985–1991 (2019).
28. Baier, S. et al. Orbital and spin dynamics of single neutrally-charged nitrogen-vacancy centers in diamond. *Phys. Rev. Lett.* **125**, 193601 (2020).
29. Zhang, Q. et al. High-fidelity single-shot readout of single electron spin in diamond with spin-to-charge conversion. *Nat. Commun.* **12**, 1529 (2021).
30. Aslam, N., Waldherr, G., Neumann, P., Jelezko, F. & Wrachtrup, J. Photo-induced ionization dynamics of the nitrogen vacancy defect in diamond investigated by single-shot charge state detection. *N. J. Phys.* **15**, 013064 (2013).
31. Poem, E. et al. Broadband noise-free optical quantum memory with neutral nitrogen-vacancy centers in diamond. *Phys. Rev. B* **91**, 205108 (2015).
32. Neuman, T. et al. A phononic interface between a superconducting quantum processor and quantum networked spin memories. *npj Quantum Inf.* **7**, 121 (2021).
33. Kurokawa, H., Yamamoto, M., Sekiguchi, Y. & Kosaka, H. Remote entanglement of superconducting qubits via solid-state spin quantum memories. *Phys. Rev. Appl.* **18**, 064039 (2022).
34. Bradley, C. E. et al. Robust quantum-network memory based on spin qubits in isotopically engineered diamond. *npj Quantum Inf.* **8**, 122 (2022).
35. Robledo, L., Bernien, H., van Weperen, I. & Hanson, R. Control and coherence of the optical transition of single nitrogen vacancy centers in diamond. *Phys. Rev. Lett.* **105**, 177403 (2010).
36. Jahnke, K. D. et al. Electron^^e2^^80^^93phonon processes of the silicon-vacancy centre in diamond. *N. J. Phys.* **17**, 043011 (2015).
37. Rogers, L. J. et al. All-optical initialization, readout, and coherent preparation of single silicon-vacancy spins in diamond. *Phys. Rev. Lett.* **113**, 263602 (2014).
38. Pingault, B. et al. All-optical formation of coherent dark states of silicon-vacancy spins in diamond. *Phys. Rev. Lett.* **113**, 263601 (2014).
39. Samkharadze, N. et al. High-kinetic-inductance superconducting nanowire resonators for circuit QED in a magnetic field. *Phys. Rev. Appl.* **5**, 044004 (2016).
40. Niepce, D., Burnett, J. & Bylander, J. High kinetic inductance NbN nanowire superinductors. *Phys. Rev. Appl.* **11**, 044014 (2019).
41. Kim, B., Kurokawa, H., Kosaka, H. & Nomura, M. Diamond optomechanical cavity with a color center for coherent microwave-to-optical quantum interfaces. *Phys. Rev. Appl.* **20**, 044037 (2023).
42. Kurokawa, H.et al. Coherent electric field control of orbital state of a neutral nitrogen-vacancy center. *figshare* https://doi.org/10.6084/m9.figshare.25017170 (2024).

Acknowledgements
H. Kosaka acknowledges the funding support from a Japan Science and Technology Agency (JST) Moonshot R&D grant (JPMJMS2062) and a JST CREST grant (JPMJCR1773). H. Kosaka also acknowledges the Ministry of Internal Affairs and Communications (MIC) for funding, research and development for construction of a global quantum cryptography network (JPMI00316), and the Japan Society for the Promotion of Science (JSPS) Grants-in-Aid for Scientific Research (20H05661, 20K20441).

Author contributions
H. Kurokawa and Y.S. designed the experiments. H. Kurokawa wrote the manuscript. K.W. and S.N performed the experiments. T.M. and H.Kato fabricated the electrical circuit. H. Kosaka supervised the project.

Competing interests
The authors declare no competing interests.

Additional information
Supplementary information The online version contains supplementary material available at https://doi.org/10.1038/s41467-024-47973-3.

Correspondence and requests for materials should be addressed to Hodaka Kurokawa or Hideo Kosaka.

Peer review information *Nature Communications* thanks Simon Baier, Mihir Bhaskar and the other, anonymous, reviewer for their contribution to the peer review of this work. A peer review file is available